Journal of Dispersion Science and Technology

ISSN: 0193-2691 (Print) 1532-2351 (Online) Journal homepage: https://www.tandfonline.com/loi/ldis20

CFD-PBM approach for the gas-liquid flow in a nanobubble generator with honeycomb structure

Fei Ren, Nao-Aki Noda, Takahiko Ueda, Yoshikazu Sano, Yasushi Takase, Toshihiko Umekage, Yuji Yonezawa & Hiroyuki Tanaka

To cite this article: Fei Ren, Nao-Aki Noda, Takahiko Ueda, Yoshikazu Sano, Yasushi Takase, Toshihiko Umekage, Yuji Yonezawa & Hiroyuki Tanaka (2019) CFD-PBM approach for the gas-liquid flow in a nanobubble generator with honeycomb structure, Journal of Dispersion Science and Technology, 40:2, 306-317, DOI: 10.1080/01932691.2018.1470009

To link to this article: https://doi.org/10.1080/01932691.2018.1470009

JOURNAL OF DISPERSION SCIENCE AND TECHNOLOGY
2019, VOL. 40, NO. 2, 306–317
https://doi.org/10.1080/01932691.2018.1470009

CFD-PBM approach for the gas-liquid flow in a nanobubble generator with honeycomb structure

Fei Ren[a], Nao-Aki Noda[a], Takahiko Ueda[a], Yoshikazu Sano[a], Yasushi Takase[a], Toshihiko Umekage[a], Yuji Yonezawa[b], and Hiroyuki Tanaka[a]

[a]Mechanical Engineering Department, Kyushu Institute of Technology, Tobata-ku, Kitakyushu-shi, Japan; [b]NANOX Co., Ltd, Nishiminato-machi, Kokurakita-ku, Kitakyusyu-shi, Japan

ABSTRACT

In recent years, nanobubble technologies have drawn great attention due to their wide applications in many fields of science and technology. From previous studies, a kind of honeycomb structure for high efficiency nanobubble generation has been proposed. In this paper, the numerical simulations of bubbly flow in the honeycomb structure were performed by using a computational fluid dynamics–population balance model (CFD-PBM) coupled model. The numerical model was based on the Eulerian multiphase model and the population balance model (PBM) was used to calculate the bubble size distribution. The bubble size distributions in the honeycomb structure under different work conditions were predicted. Two different drag force models (Schiller-Naumann model and Tomiyama model) and two different aggregation models (Luo model and turbulent aggregation model) were investigated. Both two drag models gave similar prediction of bubble number density distribution at the outlet. The results obtained from Luo model had better reflection of the trend of number density distribution. The turbulence dissipation rate ε can be used to evaluate the nanobubble generating ability. The water tank was not included in the CFD model in this work. The bubbles in the water tank should be studied in the future.

ARTICLE HISTORY
Received 26 December 2017
Accepted 13 April 2018

KEYWORDS
Bubbly flow; CFD-PBM; honeycomb; nanobubble

GRAPHICAL ABSTRACT

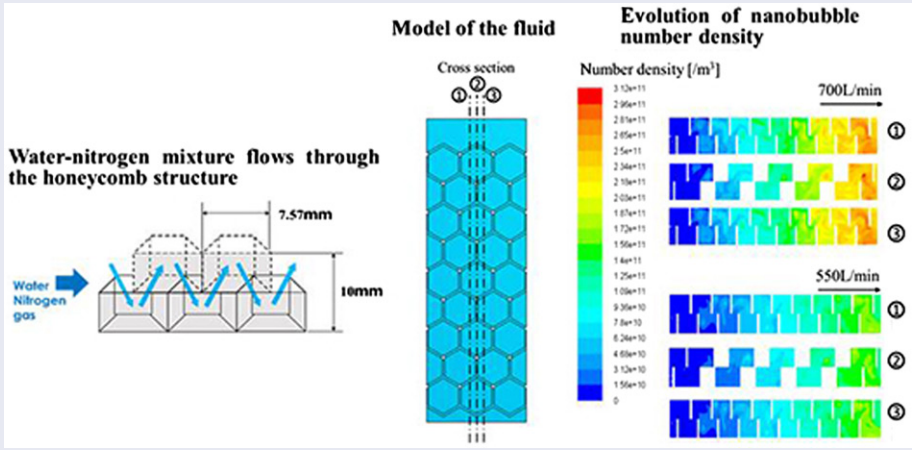

Introduction

Nanobubbles are nanoscopic gaseous cavities in aqueous solutions that have the ability to change the normal characteristics of liquids. Ordinary bubbles have diameter larger than 1 μm and quickly rise to the surface of a liquid and collapse. Nanobubbles have diameter less than 100 nm, they will randomly drift due to Brownian Motion and can remain in liquids for an extended period of time.[1–3] Nanobubbles have been widely used in varied fields,[4,5] including the improvement of t-

he dissolved oxygen (DO) for chemical and biochemical oxygen demands, reduction of suspended solids and water quality improvement.[6,7] Furthermore, in the medical field, combining with ultrasound, nanobubbles can be used as the contrast agent. Nanobubble technology is also widely used in food industry, such as seafood long term storage by using nitrogen nanobubble water circulation to reduce the dissolved oxygen

CONTACT Nao-Aki Noda noda.naoaki844@mail.kyutech.jp Kyushu Institute of Technology, Kitakyushu 804-8550, Japan
Color versions of one or more of the figures in the article can be found online at www.tandfonline.com/ldis.

(DO) and slow the progressions of oxidation and spoilage.[8] So far, many studies have been done for nanobubble generation,[5,9,10] but the bubble density and the discharge amount are insufficient for the broader applications.

Recently, a kind of honeycomb structure was designed for high efficiency nanobubble generation.[11,12] Aggregation and breakage occur together and cause a wide range of bubble sizes when the bubbles flow in the honeycomb structure. Calculation of the bubble size and number density distribution and study of the processes of aggregation and breakage in bubbly flow are very important for the evaluation and improvement of nanobubble generating ability.

Nowadays, many researches have been done on multiphase flow using computational fluid dynamics (CFD) simulations for engineering purposes.[13] The Euler–Lagrange approach [14,15] and the Euler–Euler approach[16,17] are widely used. The Euler–Lagrange approach has an advantage on clear physical description but requires high computational capacity, and it is difficult to involve the forces on the bubble deformation, breakage and aggregation.[13] For the Euler–Euler approach, the model equations have the same form for each phase, having obvious advantage on computational cost.[13]

Population balance method is widely used for particulate systems that can estimate the dynamic evolution of bubble size distribution taking into account the aggregation and breakage effects in bubbly flow.[18,19] This approach is concerned with maintaining a record of the number of bubbles initially and tracking their evolution in space over time.

A progress in the CFD simulation of bubbly flow is the coupling of the population balance method (PBM) into CFD models.[13,20–22] CFD-PBM coupled model combines the advantages of CFD to simulate the entire flow field and of the PBM to calculate the bubble size distribution, and it also takes into account the effects of bubble size on the interphase interaction, which allows it to give good prediction of the local gas-liquid interfacial area and the flow behavior in diverse flow regimes.[13,23]

So far, CFD-PBM approach is widely used in the studies of flotation column[24,25] and bubble column.[26,27] These studies provide many references on the applications of CFD-PBM approach. However, few studies have been conducted on the CFD simulation of bubble generator.

The aim of this work is to obtain a better understanding of the bubble aggregation and breakage in the new type nanobubble generator and provide valuable references to the design and improvement of nanobubble generator. In this work, the CFD-PBM coupled model along with the RNG k-ε turbulence model is used to simulate the bubble aggregation and breakage and predict the bubble number density distribution for the case of gas-liquid bubbly flow in the honeycomb structure. The nanobubble generating ability is evaluated in terms of the turbulence dissipation rate ε.

Model descriptions

Euler–Euler two-fluid model

For the bubbly flow in the honeycomb structure, the water is regarded as a continuous primary phase and the gas is regarded as a dispersed secondary phase. The continuity equation for the q^{th} phase is,

$$\frac{\partial}{\partial t}(\alpha_q \rho_q) + \nabla \cdot (\alpha_q \rho_q \vec{u}_q) = 0 \quad [1]$$

where α_q, ρ_q and $\vec{u}_q$ are the volume fraction, density and velocity of the q^{th} phase respectively. The momentum balance for the q^{th} phase is

$$\frac{\partial}{\partial t}(\alpha_q \rho_q \vec{u}_q) + \nabla \cdot (\alpha_q \rho_q \vec{u}_q \vec{u}_q) =$$

$$-\alpha_q \nabla p + \nabla \cdot \overline{\tau_q} + \alpha_q \rho_q \vec{g} + \vec{F}_{drag,q} + \vec{F}_{lift,q} + \vec{F}_{VM,q} \quad [2]$$

where $\overline{\tau_q}$, p and $\vec{g}$ are stress-strain tensor, pressure and gravity acceleration respectively of the q^{th} phase. $\vec{F}_{drag,q}$, $\vec{F}_{lift,q}$ and $\vec{F}_{VM,q}$ are drag force, lift force and virtual mass force acting on the q^{th} phase.[19]

Now we assume the phase q is the primary phase and the phase p is the secondary phase, the drag force is written as

$$\vec{F}_{drag,q} = \frac{1}{8} C_D A_i \rho_q |\vec{u}_p - \vec{u}_q| (\vec{u}_p - \vec{u}_q) \quad [3]$$

where A_i is the interfacial area, C_D is the drag coefficient, and $\vec{F}_{drag,q} = -\vec{F}_{drag,\ p}$. C_D can be calculated in terms of Reynolds number Re according to the Schiller-Naumann model,[28]

$$C_D = \begin{cases} 24(1 + 0.15\mathrm{Re}^{0.687})/Re & Re<1000 \\ 0.44 & Re>1000 \end{cases} \quad [4]$$

Another concerned drag model in this study is Tomiyama drag model.[29] The Tomiyama model is well suited to gas-liquid flows in which the bubbles can have a range of shapes. The expression of C_D is given by

$$C_D = max\left(min\left(\frac{24}{Re}(1 + 0.15\mathrm{Re}^{0.687}),\ \frac{72}{Re}\right),\ \frac{8}{3}\frac{Eo}{Eo + 4}\right) \quad [5]$$

$$Eo = \frac{g(\rho_q - \rho_p)L^2}{\sigma} \quad [6]$$

where σ is the surface tension, and L is the bubble diameter.

The virtual mass force is caused by the relative acceleration of two phases and the lift force relates to the velocity gradient in the flow field of primary phase.[19] They are described as

$$\vec{F}_{VM,q} = -0.5\alpha_p \rho_q \left(\frac{d_q \vec{u}_q}{dt} - \frac{d_p \vec{u}_p}{dt}\right) \quad [7]$$

$$\vec{F}_{lift,q} = C_l \rho_q \alpha_p (\vec{u}_q - \vec{u}_p) \times (\nabla \times \vec{u}_q) \quad [8]$$

where C_l is the lift force coefficient, d_q/dt is the phase material time derivative, and $\vec{F}_{VM,q} = -\vec{F}_{VM,p}$, $\vec{F}_{lift,q} = -\vec{F}_{lift,p}$. The Tomiyama lift force model[30,31] is concerned in this work. The expression of C_l, lightly modified by Frank et al,[32] is given by

$$C_l = \begin{cases} min\left[0.288tanh(0.121Re_p), f(Eo')\right] & Eo' \le 4 \\ f(Eo') & 4 < Eo' \le 10 \\ -0.27 & 10 < Eo' \end{cases} \quad [9]$$

Where

$$f(Eo') = 0.00105Eo'^3 - 0.0159Eo'^2 - 0.0204Eo' + 0.474 \quad [10]$$

Re_p is Reynolds number of bubble, Eo' is Eötvös number. They are given by,

$$Re_p = \frac{\rho_q|\vec{u}_q - \vec{u}_p|L}{\mu_q} \quad [11]$$

$$Eo' = \frac{g(\rho_q - \rho_p)L_h^2}{\sigma} \quad [12]$$

$$L_h = L(1 + 0.163\mathrm{Eo}^{0.757})^{1/3} \quad [13]$$

$$Eo = \frac{g(\rho_q - \rho_p)L^2}{\sigma} \quad [14]$$

where μ_q is the shear viscosity of phase q, L_h is the long axis of the deformable bubble, σ is the surface tension, and L is the bubble diameter.

Laborde-Boutet et al.,[33] investigated the available choices for RANS-based turbulence models following nine different options, i.e., three formulations of the k–ε model (Standard, RNG, Realizable) combined with three different modalities to account for gas-phase effects (Dispersed, Dispersed + Bubble Induced Turbulence, Per-Phase). RNG k-ε model can obtain a better estimation of breakage rates during the execution of bubble-population balance.[33] RNG k–ε models[33,34] were recommended for the execution of bubble population balance models. The k and ε for continuous phase are computed by the follows,

$$\frac{\partial}{\partial t}(\alpha_q\rho_q k_q) + \nabla\cdot(\alpha_q\rho_q\vec{u}_q k_q) =$$

$$\nabla\cdot\left(\alpha_q\left(\mu_q + \frac{\mu_{t,q}}{\sigma_k}\right)\nabla k_q\right) + \alpha_q G_{k,q} - \alpha_q\rho_q\varepsilon_q \quad [15]$$

And

$$\frac{\partial}{\partial t}(\alpha_q\rho_q\varepsilon_q) + \nabla\cdot(\alpha_q\rho_q\vec{u}_q\varepsilon_q) =$$

$$\nabla\cdot\left(\alpha_q\left(\mu_q + \frac{\mu_{t,q}}{\sigma_\varepsilon}\right)\nabla\varepsilon_q\right) + \alpha_q\frac{\varepsilon_q}{k_q}(C_{1\varepsilon}G_{k,q} - C_{2\varepsilon}\rho_q\varepsilon_q) \quad [16]$$

In these equations, σ_k and σ_ε are the turbulent Prandtl numbers for k and ε, respectively, and σ_k=σ_ε=0.7194. $C_{1\varepsilon}$ and $C_{2\varepsilon}$ are constants, and $C_{1\varepsilon}$=1.42, $C_{2\varepsilon}$=1.68. $G_{k,q}$ is the production of turbulent kinetic energy, this term is defined as

$$G_{k,q} = \rho_q C_\mu\frac{k_q^2}{\varepsilon_q}S^2 \quad [17]$$

where S is the modulus of the mean rate-of-strain tensor.

For the dispersed phase, time and length scales that characterize the motion are used to evaluate dispersion coefficients, correlation functions, and the turbulent kinetic energy. The influence of the dispersed phase on the turbulence of the liquid phase is taken into account with Sato's additional term.[35] In the high-Reynolds number limit, the turbulent viscosity $\mu_{t,q}$ is computed as

$$\mu_{t,q} = \rho_q\nu_q \quad [18]$$

$$\nu_q = C_\mu\frac{k_q^2}{\varepsilon_q} + C_{\mu,p}\alpha_p L|\vec{u}_p - \vec{u}_q| \quad [19]$$

where C_μ=0.0845, L is the bubble diameter and $C_{\mu,p}$=0.6. The kinematic viscosity ν_p for the dispersed secondary phase is defined as ν_p=ν_q.

Discrete population balance model

The discrete population balance method can compute the bubble size distribution directly by discretizing the bubble population with a relatively small number of size intervals. The size distribution that is coupled with CFD can be computed.

Assuming that the bubbles are spherical, the volume fraction of gas phase is given by

$$\alpha_p(\vec{x},t) = \int_0^{+\infty} n(\vec{x},\Phi,t)\frac{\pi}{6}L^3 dL \quad [20]$$

where L is the bubble diameter and $n(\vec{x},\Phi,\mathrm{t})$ is the number density function. The "external coordinates" $(\vec{x})$ denote the spatial position of the bubble and "internal coordinates" (Φ) denote the bubble volume. The transport equation for $n(\vec{x},\Phi,\mathrm{t})$ is given as[19,36]

$$\frac{\partial}{\partial t}[n(V,t)] + \nabla\cdot[\vec{u}n(V,t)] = B_{ag}(V,t)$$

$$+B_{br}(V,t) - D_{ag}(V,t) - D_{br}(V,t) \quad [21]$$

Aggregation kernel

Bubble aggregation is caused by bubble collisions. These collisions may be caused by various mechanisms, such as the turbulence of the liquid and Brownian motion. Brownian motion is not considered in this work because the gas volume fraction is very low, less than 1%.

The birth rate of bubbles of volume V due to aggregation is given by[36]

$$B_{ag} = \frac{1}{2}\int_0^V \Omega_{ag}(V - V', V')n(V - V', t)n(V', t)dV' \quad [22]$$

where bubbles of volume V-V' aggregate with bubbles of volume V' to form bubbles of volume V.

The death rate of bubbles of volume V due to aggregation is given by[36]

$$D_{ag} = \int_0^\infty \Omega_{ag}(V, V')n(V, t)n(V', t)dV' \quad [23]$$

where Ω_{ag} is called aggregation kernel (m^3/s).

The aggregation kernel is defined by Luo model[36,37] as the bubble formation rate due to binary collision between bubbles of volumes V_i and V_j.

$$\Omega_{ag}(V_i, V_j) = \omega_{ag}(V_i, V_j)P_{ag}(V_i, V_j) \quad [24]$$

where ω_{ag} is the collision frequency,

$$\omega_{ag}(V_i, V_j) = \frac{\pi}{4}(L_i + L_j)^2 n_i n_j \overline{u}_{ij} \quad [25]$$

where $\overline{u}_{ij}$ is the characteristic velocity of two colliding bubbles with diameter L_i and L_j and number densities n_i and n_j.

$$\overline{u}_{ij} = 1.43\varepsilon^{1/3}(L_i^{2/3} + L_j^{2/3})^{1/2} \quad [26]$$

where ε is the turbulence dissipation.

The probability of aggregation caused by the collision, P_{ag}, is given as

$$P_{ag} = \exp\left\{-c_1 \frac{\left[0.75(1 + L_i^2/L_j^2)(1 + L_i^3/L_j^3)\right]^2}{(\rho_p/\rho_q + 0.5)^{1/2}(1 + L_i/L_j)^3}\mathrm{We}^{1/2}\right\} \quad [27]$$

where c_1 is a constant of order unity, L_i/L_j is the bubble size ratio and ρ_p/ρ_q is the density ratio of bubble and liquid. *We* is the Weber number as following,

$$We = \frac{\rho_q L_i(\overline{u}_{ij})^2}{\sigma} \quad [28]$$

where σ is the interface tension.

Another aggregation model concerned in this study is called turbulent aggregation model.[36] In turbulent flow, eddies appear due to the turbulence. The largest eddies transfer energy to the smallest eddies, and the energy is dissipated through viscous interactions. The size of the smallest eddies is the Kolmogorov microscale, $\eta = (\nu^3/\varepsilon)^{1/4}$, where ν is the kinematic viscosity and ε is the turbulent energy dissipation rate.

When bubbles are smaller than the Kolmogorov microscale, bubble collisions are mainly due to the local shear within the eddy. In the work by Saffman and Turner,[38] the aggregation rate is given as,

$$\Omega_{ag}(L_i, L_j) = \varsigma_T\sqrt{\frac{8\pi}{15}}\dot{\gamma}\frac{(L_i + L_j)^3}{8} \quad [29]$$

where ς_T is the capture efficiency coefficient of turbulent collision, and $\dot{\gamma}$ is the shear rate: $\dot{\gamma} = \varepsilon^{0.5}/\nu$.

When bubbles are larger than the Kolmogorov microscale, they are dragged by velocity fluctuations in the flow field, the aggregation rate in this case is given by Abrahamson's model,[39]

$$\Omega_{\mathrm{ag}}(L_i, L_j) = \varsigma_T 2^{3/2}\sqrt{\pi}\frac{(L_i + L_j)^2}{4}\sqrt{\left(U_i^2 + U_j^2\right)} \quad [30]$$

where U_i^2 is the mean squared velocity for bubble *i*.

Higashitani et al.[40] proposed the empirical capture efficiency coefficient of turbulent collision:

$$\varsigma_T = 0.732\left(\frac{5}{N_T}\right)^{0.242};\ N_T \geq 5 \quad [31]$$

where N_T is the ratio between the viscous force and the Van der Waals force,

$$N_T = \frac{6\pi\mu(L_i + L_j)^3\dot{\lambda}}{8H} \quad [32]$$

where H is the Hamaker constant, and $\dot{\lambda}$ is the rate of deformation,

$$\dot{\lambda} = \left(\frac{4\varepsilon}{15\pi\nu}\right)^{0.5} \quad [33]$$

Luo breakage kernel

The birth rate of bubbles of volume V due to breakage is given by[19,36]

$$B_{br} = \int_{\Omega_V} c_b g(V')\beta(V|V')n(V', t)dV' \quad [34]$$

where $g(V')$ is the breakage frequency, that is the fraction of bubbles of volume V' breaking per unit time. $\beta(V|V')$ is the daughter size distribution, which denotes the probability density function of bubbles breaking from volume V' to V, c_b is the number of daughter bubbles from per original bubble, and c_b=2 for binary breakage.[19,36]

The death rate due to breakage for bubbles of volume V is given by[19,36]

$$D_{br} = g(V)n(V, t) \quad [35]$$

The Luo breakage model[37] includes both the breakage frequency and the probability density function of breaking bubbles. The breakage kernel Ω_{br} is given as

$$\Omega_{br}(V, V') = g(V')\beta(V|V')\ [m^{-3}s^{-1}] \quad [36]$$

where V is the volume of daughter bubble and V' is the volume of original bubble.

The general form of Ω_{br} is the integral over the eddy size l. Assuming that the eddy with size l hits the bubble with diameter L, the eddy size l can be normalized as $\xi = l/L$, then Ω_{br} is expressed as,[19,36]

$$\Omega_{br}(V, V') = 0.923(1 - \alpha_p)\left(\frac{\varepsilon}{L^2}\right)^{1/3}\int_{\xi_{\min}}^1 \frac{(1 + \xi)^2}{\xi^{11/3}}\exp\left(-b\xi^{-11/3}\right)d\xi \quad [37]$$

where b is modeled as

$$b = 12\frac{\left[f_{bv}^{2/3} + (1 - f_{bv})^{2/3} - 1\right]\sigma}{2.047\rho_q\varepsilon^{2/3}L^{5/3}} \quad [38]$$

where the breakage volume fraction f_{bv} is expressed as $f_{bv=}V/V'$. The breakage kernel is symmetric about f_{bv}=0.5 for binary breakage.

Numerical method for PBM

The population balance equation can be written in terms of volume fraction of bubble size i,[19,36]

$$\frac{\partial(\rho_p \alpha_i)}{\partial t} + \nabla \cdot \left(\rho_p \vec{u}_i \alpha_i\right) = \rho_p V_i (B_{ag,i} - D_{ag,i} + B_{br,i} - D_{br,i}) \quad [39]$$

where ρ_p is the density of the secondary phase and α_i is the volume fraction of the bubble size i defined as

$$\alpha_i = N_i V_i \;\; i = 0, 1, \ldots, N-1 \quad [40]$$

where V_i is the volume of bubble size i, and N_i is given by

$$N_i t = \int_{V_i}^{V_{i+1}} n(V,t) dV \quad [41]$$

In this work, the breakage formulation for the discrete method is given by Hagesather[41] and an assumption is that the smallest bubble class does not break further.

Nanobubble generating device and experimental details

From previous studies, a kind of honeycomb structure for high efficiency nanobubble generation was proposed. Figure 1 shows the bubble generating device equipped with parallel honeycomb structure units. The device is placed in the water in a tank and the water and nitrogen gas are pumped into the bubble generator together as is shown in Figure 1a. There are 15 honeycomb structure units placed in parallel inside the bubble generator as is shown in Figure 1b. Figure 2a shows the composition of the honeycomb structure unit. One honeycomb unit has four plates, two honeycomb plates (②③) and two cover plates (①④), covered each other, so that the complex crisscross flow channels are formed in the honeycomb unit. The flow path in this honeycomb structure is shown in Figure 2b. High turbulence will occur when the gas-liquid mixture flows through the honeycomb unit. The aggregation and breakage happen in the turbulent flow and cause a wide range bubble size distribution. Figure 2c is the picture of honeycomb plates (②③) and Figure 2d shows the combined honeycomb plates. Moreover, the length of the side of the hexagon is 3.5 mm and the thickness of the wall between two hexagons is 0.5 mm.

Nanobubbles flow out of the generator and then stay in the tank. The nanobubble number density in the tank is measured from the sample taken from the tank. The nanoparticle analyzer, Nano Sight LM10-HS,[42,43] is used to measure the nanobubble density of the sample. Figure 3 shows the principle of Nano Sight LM10-HS. Irradiating a laser beam in the horizontal direction in the sample liquid, the side-scattered light from the nanobubbles are visualized by the objective lens, the movement trajectory of each bubble is displayed on the computer. Tracking Brownian motion of all bubbles recognized on the screen and using the Stokes-Einstein equation, the bubble size is obtained from the moving velocity of the bubble.

The details of the experimental device are shown in Table 1. The main purpose of this device is to generate nitrogen nanobubbles and use the nitrogen nanobubbles to reduce the dissolved oxygen (DO). The experimental results of different flow rates are shown in Table 2. Here, the gas-liquid mixture flow rate is controlled by the pump power and the gas flow rate is a constant 5L/min in the experiment. From Table 2 it can be seen that the DO decreases and the bubble number density increases over the time. Not all of the particles are nitrogen nanobubbles because it is hard to distinguish what type of the particle might be. However, we can believe that most of the increased particles are nitrogen bubbles generated by the device, and these bubbles make the DO lower. Moreover, the device can generate more bubbles with higher flow rate. The bubble size and number density distribution will be analyzed in the next chapter.

Numerical details

In this work, all computations were performed using the commercial CFD software ANSYS FLUENT 16.2. Because of the symmetry, only a part of one honeycomb structure unit will be modeled to simplify the CFD analysis, as is shown in Figure 4. According to the device in the experiment, the

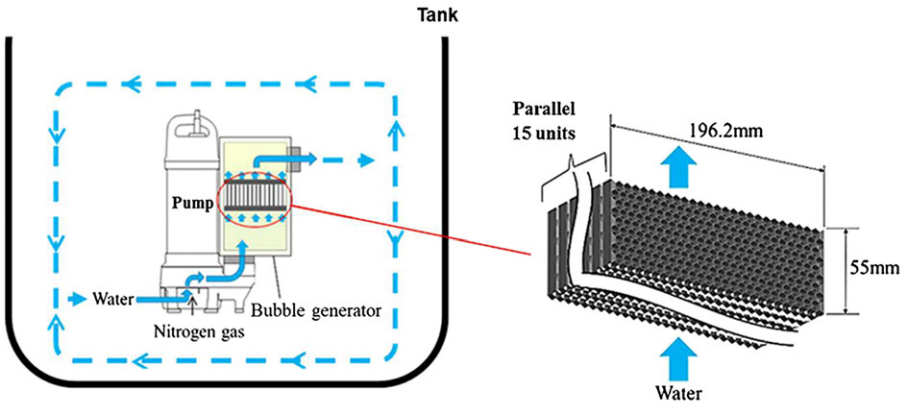

Figure 1. Nitrogen nanobubble generating device.

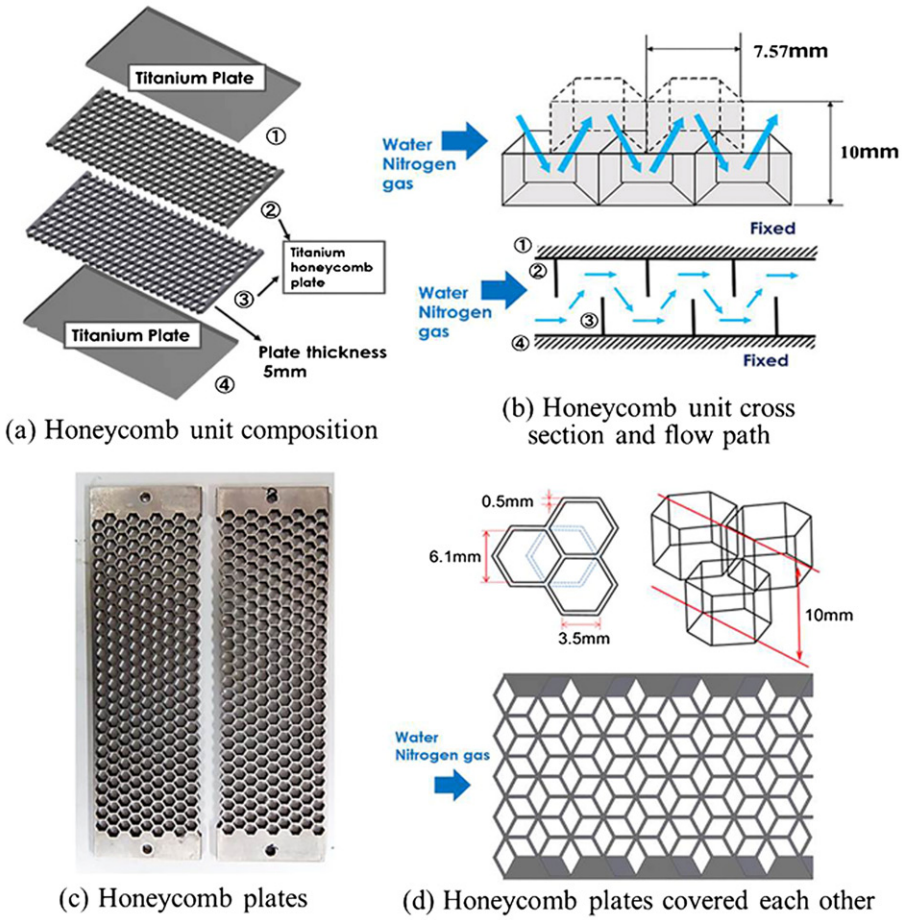

Figure 2. Honeycomb structure.

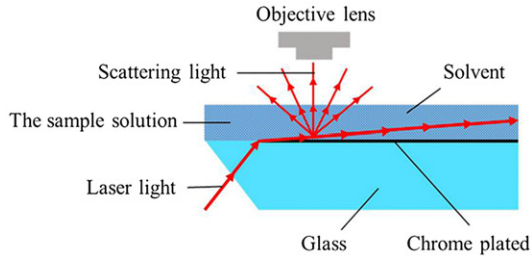

Figure 3. Schematic of Nano Sight LM10-HS.

length of the side of the hexagon is 3.5 mm and the thickness of the wall between two hexagons is 0.5 mm. Pressure-outlet boundary condition is applied. Along the walls, no-slip boundary conditions are adopted. The symmetry boundary conditions are applied on the two sides of the model. The inlet velocities are 0.456m/s and 0.358m/s according to the flow rates 700L/min and 550L/min. The gas flow rate is a constant 5L/min, therefore the gas volume fractions at the inlet are 0.00714 and 0.00909 when the flow rates are 700L/min and 550L/min. An assumption is that the gas phase has the same velocity as the liquid phase at the inlet because the gas volume fraction is small and the bubble size is small. The number of bubble bins is specified 10, Table 3 presents the diameters of bubble bins tracked in this simulation. Nano Sight LM10-HS can detect the bobbles with the

Table 1. Details of the experimental device.

Item	Specification
Pump	Submersible pump(80TM23.7)
Output [kW]	3.7, (60Hz)
Tank [mm]	1580 × 1100 × 600
Water and amount [kg]	Tap water, 1000
Gas	Nitrogen
Flow rate [L/min]	5.0

diameter only from 0 to 1000 nm, 7 of 10 bins are set in this diameter range, this is to focus on the small bubbles and easily compare with the experimental results.

The tank is not included in the model. An extension, as is shown in Figure 4, is added to the real outlet of honeycomb structure, the pressure outlet is defined at the end of the extension. The results at the real outlet are used in this work in order to avoid the possible influences and errors caused by the pressure-outlet boundary condition, such as the reversed flow. In this work, there is no gas in the domain at the beginning and bin 8 (1280 nm) is chosen as the initial size at the inlet. The initial size is estimated according to the inlet geometrical dimension and gas volume fraction because the real bubble size distribution at the inlet is unknown. Furthermore, bin 7 and bin 9 are tested respectively as the initial sizes and similar size distribution can be obtained at the outlet. In this work, hexahedral grids with different sizes (number of elements: 843129 and 1388161) are constructed to ensure independence of

Table 2. Experimental results of DO.

	Flow rate 700 L/min		Flow rate 550 L/min	
Time (minutes)	DO [mg/L]	Bubble (or particle) number density [$\times 10^8$/mL]	DO [mg/L]	Bubble (or particle) number density [$\times 10^8$/mL]
0	10.4	0.37	10.14	0.41
10	4.4	0.82	7.79	0.43
20	2.5	1.12	6.7	0.88
30	1.7	1.72	5.5	0.94

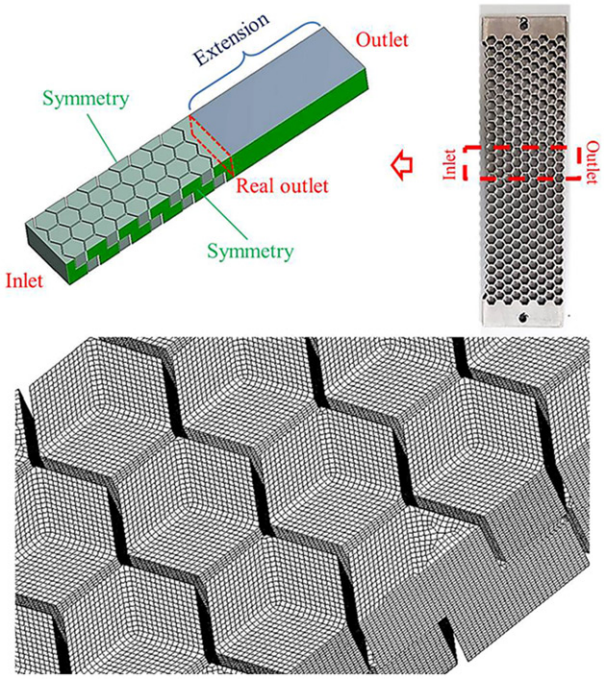

Figure 4. Simplified honeycomb unit model and the grids of honeycomb cells.

Table 3. Diameter of each bubble bin.

Bubble bin number	1	2	3	4	5	6	7	8	9	10
Mean bubble diameter (nm)	10	20	40	80	160	320	640	1280	2560	5120

obtained results on mesh density. The computation starts with the first-order discretization scheme and then switches to the second-order scheme after several iterations. The percentage of change of the solution in both cases is small and there are no significant differences in the results. The overall pressure drops are 0.15 MPa and 0.09 MPa when the flow rates are 700L/min and 550L/min, coinciding with the experimental data. Therefore, the mesh consisting 843129 numerical meshes is chosen for further simulations.

In the next discussion, in a simplified way we refer to the Schiller-Naumann drag model as model SN, Tomiyama drag model as model T, Luo aggregation model as model Luo, and turbulent aggregation model as model Turb. Figure 5 shows the initial bubble number density distribution of different flow rates at the inlet. Due to the fixed gas flow rate 5L/min, the gas volume fraction is smaller when the mixture flow rate is high, the bubble number density when flow rate is 700L/min is smaller than that when flow rate is 550L/min. Figure 6 shows the simulated bubble number density at the outlet with different drag models and Figure 7 shows the number density distribution of the bubbles with diameter less than 350 nm. Luo model is used in Figures 6 and 7. It is

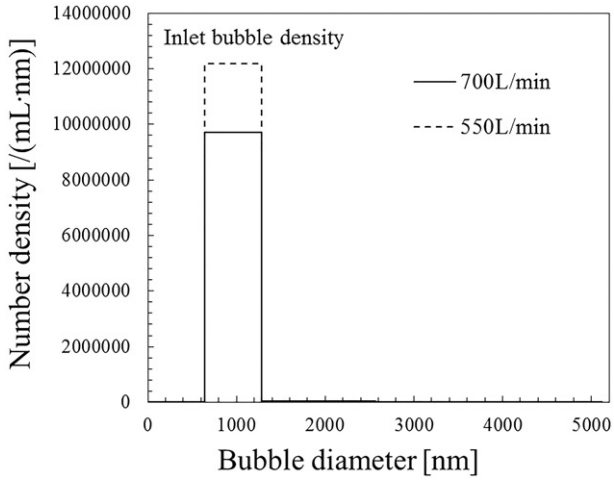

Figure 5. Initial bubble number density distribution at the inlet.

found that both SN model and T model give similar prediction of bubble number density distribution at the outlet. When Luo aggregation model is used, the number of bubbles with diameter larger than 1000 nm becomes higher significantly at the outlet, which means the majority of the bubbles at inlet aggregate into the larger bubbles after flowing through the honeycomb structure. In Figure 7, more small bubbles are generated when flow rate is 700L/min. Figure 8 shows the comparison of Luo aggregation model and turbulent aggregation model, SN drag model is used in this case. The details of bubbles with diameter less than 350 nm are shown in the right side in Figure 8. When turbulence aggregation model is used, the number of bubbles with diameter about 1000 nm is large at the outlet. For the small bubbles, the bubbles with diameter about 10 nm have the largest number.

The large bubbles in the tank quickly rise to the surface of water and collapse, only the tiny bubbles remain in the water tank and are detected by Nano Sight LM10-HS. Figure 9 shows the bubble number density distribution in the tank. The simulation result is obtained by

$$N_{pbm}^{tank} = \frac{N_{pbm}^{outlet} \cdot Q_{total} \cdot t}{V_{water}^{tank}} \quad [42]$$

where N_{pbm}^{outlet} is the number density at the outlet as is shown in Figures 7 and 8, Q_{total} is the flow rate (700L/min and 550L/min), t is the experiment time (30 minute) and V_{water}^{tank} is the volume of water in the tank ($1m^3$). N_{pbm}^{tank} denotes the number density of the bubbles generated from the device, the original bubbles (or other particles) in the water tank when t = 0 minute are not included. The 30-minute experimental result includes the original bubbles (or other particles).

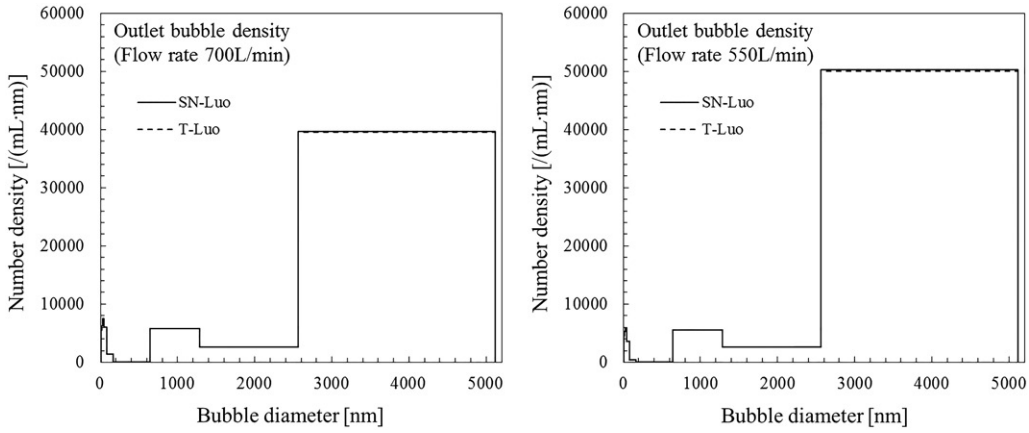

Figure 6. Simulated bubble number density distribution at the outlet with different drag models.

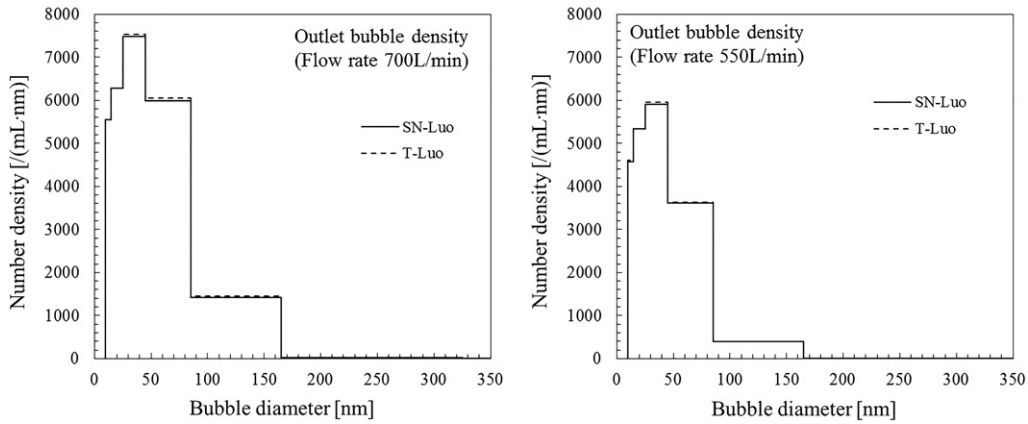

Figure 7. The number density distribution of the bubbles with size less than 350 nm.

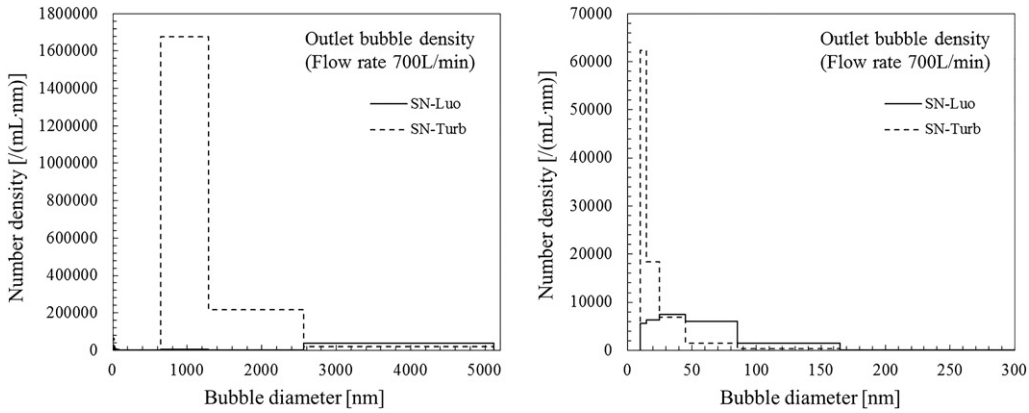

Figure 8. Simulated bubble number density distribution at the outlet with different aggregation models.

In Figure 9, the bubble number density distributions in the tank from two different aggregation models are compared with experimental data. A large difference can be found between the results obtained from turbulent aggregation model and the experimental data, and the results obtained from Luo model have much better reflection of the trend of number density distribution. In the range of 0 nm to 350 nm, only six bin sizes are calculated because of the limit of computer power, the more accurate solution may be obtained by calculating more bubble bins using more computing resource. In the experiment, the number of bubbles with diameter of 70 nm is the largest when the flow rate is 550L/min, the number of bubbles with diameter of 82 nm is the largest when the flow rate is 700L/min. Table 4 shows the number densities of the bubbles with diameters of 70 nm and 82 nm. Simulation results are obtained by interpolation from the results of six bin sizes shown in Figure 9, Luo aggregation model is used here. The original particles should not be counted so that the effective number density can be calculated by subtracting the 0-minute experimental

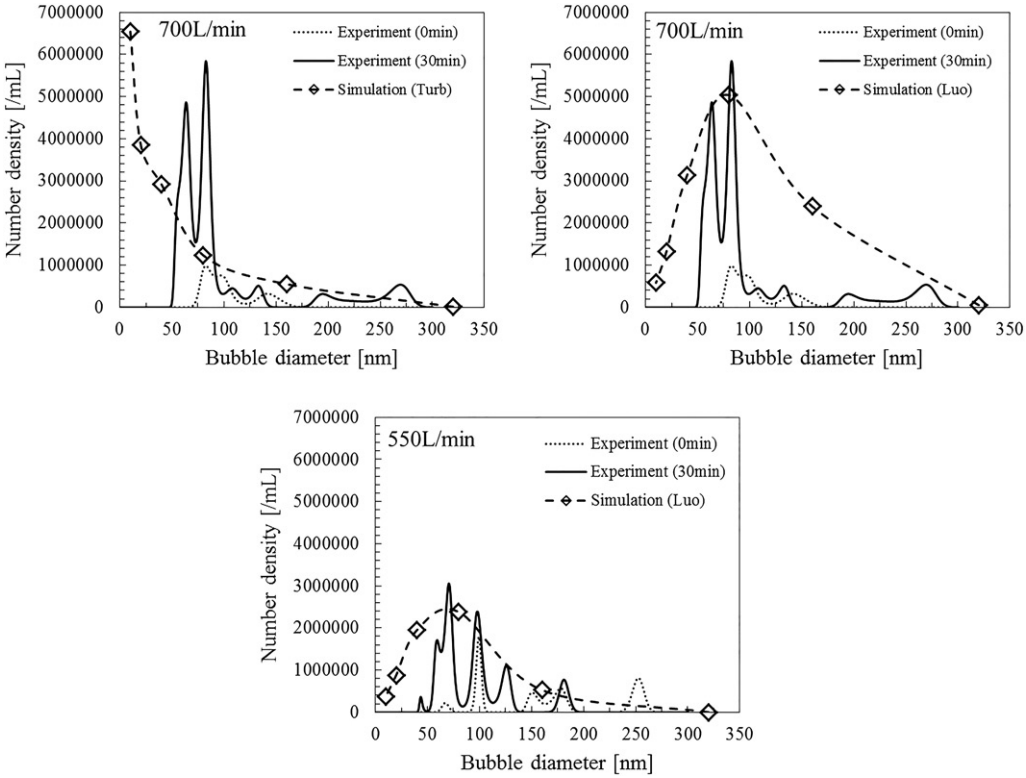

Figure 9. Bubble number density distribution in the tank.

Table 4. Number density details of the bubbles with diameters of 70 nm and 82 nm.

	Flow rate 550L/min Bubble size 70nm	Flow rate 700L/min Bubble size 82nm
Experimental result		
0 minute	96727/mL	989257/mL
30 minutes	3056609/mL	5843111/mL
30 minutes–0 minute	2959882/mL	4853854/mL
Simulation result (SN-Luo)	2608186/mL	4999691/mL
Error	12%	2%

result from the 30-minute experimental result. It can be found in Table 4 that the simulation result can accurately predict what bubble size is the most predominant and the number of bubbles with this predominant size.

Turbulent breakup of bubbles

The processes of aggregation and breakage in the bubbly flow may be influenced by many factors, such as turbulence, Brownian motion and mass transfer. In this work, the gas concentration in honeycomb structure is very low, less than 1%, bubbles flow through the honeycomb structure in a short time and have no chemical reaction with water. Therefore, turbulence may play the leading role in the aggregation and breakage processes. The breakage process in turbulence should be concerned for the nanobubble generation.

The first work on the turbulent breakup of bubbles was due to Kolmogorov.[44] The size of bubbles in turbulent flow is determined by the forces acting on the bubble. In low viscosity liquids the deformation of the bubble is mainly due to force from liquid velocity fluctuation acting over distance of the order of the bubble diameter, L. The surface tension acting at the gas-liquid interface causes restoring force resisting the deformation of the bubble. The ratio of these two forces is known as the Weber number, as is shown in Equation (28). The Weber number can be used to predict a maximum stable bubble diameter L_m, by assuming that a bubble will split once a critical Weber number, We_c, is reached,[45]

$$\mathrm{We}_c = \frac{\rho_q L_m \overline{u}^2}{\sigma} \qquad [43]$$

If the bubble is smaller than the turbulent macroscale but larger than the turbulent microscale, the eddies responsible for breakup are isotropic and lie within the inertial subrange such that their kinetic energy is independent of viscosity and follows the Kolmogorov energy distribution law,[44,45]

$$\overline{u}^2 = 2\left(\frac{\varepsilon L}{\rho_q}\right)^{2/3} \qquad [44]$$

Substituting this expression into Equation (43), the maximum stable bubble diameter can be expressed as,[45]

$$L_m = \left(\frac{\mathrm{We}_c \sigma}{2}\right)^{3/5} \rho_q^{-1/5} \varepsilon^{-2/5} \qquad [45]$$

A commonly accepted idea is that bubbles whose $We > We_c$ are unstable and ultimately break up in a given time. Unfortunately, the knowledge of the critical Weber number We_c is clearly insufficient.

According to Equation (45), the maximum stable bubble diameter L_m will be small if ε is large. Large ε means a good ability to generate small bubbles. Figure 10 shows the

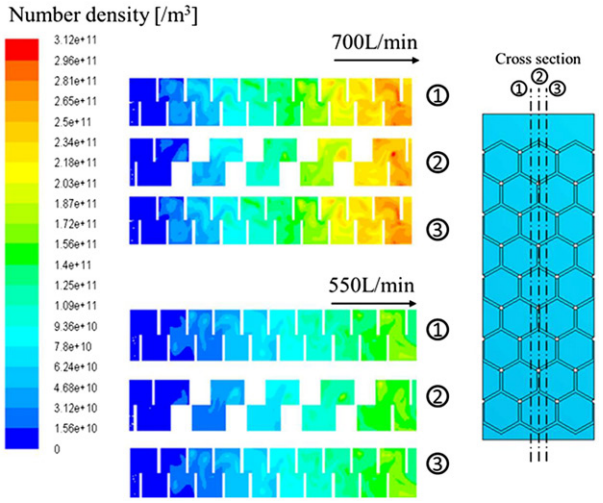

Figure 10. The number density distribution of the bubbles with diameter 80 nm.

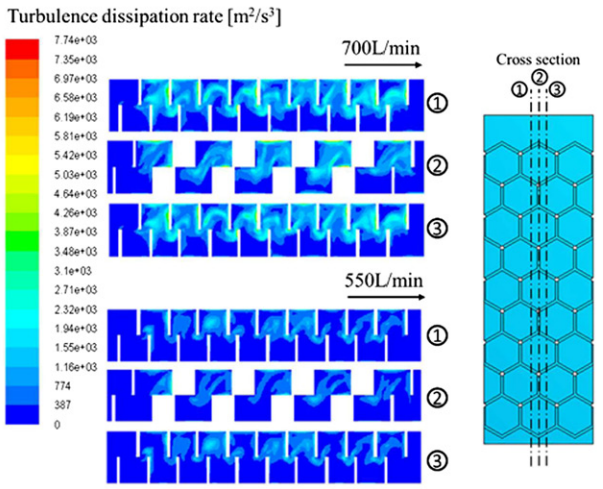

Figure 11. The turbulence dissipation rate distribution.

number density distribution of the bubbles with diameter 80 nm (bin 4) in the honeycomb structure. Figure 11 shows the turbulence dissipation rate distribution. The bubbles appear in the zone of high ε. The honeycomb structure can produce several high-ε zones and the number of tiny bubbles keeps increasing in this repeated flow channel. In Figures 7 and 9 it is found that more small bubbles are generated when flow rate is 700L/min, this is because ε is higher when flow rate is 700L/min as shown in Figure 11.

Conclusions and perspective

In this work, the bubble aggregation and breakage processes in bubbly flow in honeycomb structure were studied. The bubble aggregation and breakage in turbulence were simulated by using the CFD-PBM coupled model along with the RNG k-ε turbulence model. The bubble number density distributions were predicted by using different drag force models and aggregation models.

Schiller-Naumann and Tomiyama drag models give similar prediction of bubble number density distribution. The results obtained from Luo aggregation model have better reflection of the trend of number density distribution than the results from turbulent aggregation model. Moreover, the results from Luo aggregation model can accurately predict the predominant bubble size and the number density of bubbles with this predominant size.

More small bubbles can be generated when turbulence dissipation rate ε is high, ε can be used to evaluate the nanobubble generating ability.

The water tank was not included in the CFD model in this work. In fact, bubbles may continue to aggregate and break after flowing out of the generator. The aggregation and breakage processes in the tank may be very different, Brownian movement and mass transfer may play important roles because of the increasing gas concentration and low velocity. The results of this work can be used as the initial conditions for the simulation of the tank in the future.

Disclosure statement

No potential conflict of interest was reported by the authors.

Funding

This work was supported by the Ministry of Economy, Trade and Industry, METI Strategic Foundational Technology Improvement Support Operation under Grant number 20160401 Kyushu 170.

References

[1] Fukushi, K.; Matsui, Y.; Tambo, N. Dissolved Air Flotation: Experiments and Kinetic Analysis. *J. Water. SRT-Aqua*. **1998**, *47*, 76–86.

[2] Onari, H.; Saga, T.; Watanabe, K.; Maeda, K.; Matsuo, K. High Functional Characteristics of Micro-Bubbles and Water Purification. *Resour. Process*. **1999**, *46*, 238–244. DOI:10.4144/rpsj1986.46.238

[3] Kakuta, I. Effective Utilization of Micro- and Nano-Bubble Technology on Environmental Improvement, Promotion of Health and Growth Rate of Organisms, Food Safety, and Medical Therapy. *Bull. Soc. Sea Water Sci. Jpn*. **2006**, *60*, 160–163. (in Japanese).

[4] Tusge, H. Fundamentals of Microbubbles and Nanobubbles. *Bull. Soc. Sea Water Sci. Jpn*. **2010**, *64*, 4–10. (in Japanese)

[5] Takahashi, M. Fundamental Properties and Technical Applications of Microbubbles. Presented at 2nd International Symposium on Application of High-voltage, Plasmas & Micro/Nano Bubbles to Agriculture and Aquaculture, Chiang Mai, Thailand, July 26, 2017.

[6] Michioku, K.; Kanda, T.; Ohnari, H.; Nishikawa, T.; Matsuo, K.; Kido, T. A Preliminary Experiment on Reservoir Water Purification by Using a Micro-Bubble Aeration System. *Proc. Hydraul. Eng*. **2000**, *44*, 1119–1124. (in Japanese) DOI:10.2208/prohe.44.1119

[7] Hasegawa, H.; Masaki, Y.; Matsuuchi, K.; Yoshida, Y. Micro-Bubble Generation by Using Pipe with Slits. *Trans. JSMET*. **2006**, *72*, 2242–2248. DOI:10.1299/kikaib.72.2242

[8] Hiraki, K. Efficient Long Term Storage Technology of Seafood Using Nitrogen Nanobubbles. *Latest Technol. Microbubbles NTS Inc*. **2014**, *2*, 177–183. (in Japanese).

[9] Tusge, H. *The latest technology on microbubbles and nanobubbles II*; CMC Publishing Co.,Ltd: Frankfurt, 2010.

[10] Sadatomi, M.; Kawahara, A.; Kano, K.; Ohtomo, A. Performance of a New Micro-Bubble Generator with a Spherical Body in a

Flowing Water Tube. *Exp. Therm. Fluid. Sci.* **2005**, *29*, 615–623. DOI:10.1016/j.expthermflusci.2004.08.006

[11] Kudo, Y.; Hiraki, K. Characteristics Comparison of the Honeycomb Mixing Device by considering the Mixing Energy in the Gas-Liquid Mixing. *Proc. Symp. Micro-Nano Sci. Technol.* **2011**, *3*, 26–27.

[12] Noda, N.-A.; Ren, F.; Yamamoto, W.; Ueda, T.; Sano, Y.; Chen, D.-H.; Takase, Y.; Yonezawa, Y. Design and Performance of Honeycomb Structure for Nanobubbles Generating Apparatus. *J. Jpn. Soc. Des. Eng.* **2018**, *53*, 111–126.

[13] Liang, X.-F.; Pan, H.; Su, Y.-H.; Luo, Z.-H. CFD-PBM Approach with Modified Drag Model for the Gas–Liquid Flow in a Bubble Column. *Chem. Eng. Res. Des.* **2016**, *112*, 88–102. DOI:10.1016/j.cherd.2016.06.014

[14] Delnoij, E.; Lammers, F.; Kuipers, J.; Van Swaaij, W. Dynamic Simulation of Dispersed Gas–Liquid Two-Phase Flow Using a Discrete Bubble Model. *Chem. Eng. Sci.* **1997**, *52*, 1429–1458. DOI:10.1016/S0009-2509(96)00515-5

[15] Sokolichin, A.; Eigenberger, G.; Lapin, A.; Lübert, A. Dynamic Numerical Simulation of Gas–Liquid Two-Phase Flows Euler/Euler versus Euler/Lagrange. *Chem. Eng. Sci.* **1997**, *52*, 611–626. DOI:10.1016/S0009-2509(96)00425-3

[16] Drew, D. Mathematical Modeling of Two-Phase Flow. *Annu. Rev. Fluid Mech.* **1983**, *15*, 261–291. DOI:10.1146/annurev.fl.15.010183.001401

[17] Krishna, R.; Urseanu, M.-I.; Van Baten, J.-M.; Ellenberger, J. Influence of Scale on the Hydrodynamics of Bubble Columns Operating in the Churn-Turbulent Regime: Experiments Vs. Eulerian Simulations. *Chem. Eng. Sci.* **1999**, *54*, 4903–4911. DOI:10.1016/S0009-2509(99)00211-0

[18] Wang, T.-F.; Wang, J.-F.; Jin, Y. Population Balance Model for Gas − Liquid Flows: Influence of Bubble Coalescence and Breakup Models. *Ind. Eng. Chem. Res.* **2005**, *44*, 7540–7549. DOI:10.1021/ie0489002

[19] Li, L.-M.; Liu, Z.-Q.; Li, B.-K.; Matsuura, H.; Tsukihashi, F. Water Model and CFD-PBM Coupled Model of Gas-Liquid-Slag Three-Phase Flow in Ladle Metallurgy. *ISIJ. Int.* **2015**, *55*, 1337–1346. DOI:10.2355/isijinternational.55.1337

[20] Duan, X.-Y.; Cheung, S. C. P.; Yeoh, G.-H.; Tu, J.-Y.; Krepper, E.; Lucas, D. Gas–Liquid Flows in Medium and Large Vertical Pipes. *Chem. Eng. Sci.* **2011**, *66*, 872–883. DOI:10.1016/j.ces.2010.11.031

[21] Wang, T.; Wang, J. Numerical Simulations of Gas–Liquid Mass Transfer in Bubble Columns with a CFD–PBM Coupled Model. *Chem. Eng. Sci.* **2007**, *62*, 7107–7118. DOI:10.1016/j.ces.2007.08.033

[22] Wang, T.; Wang, J.; Jin, Y. A CFD-PBM Coupled Model for Gas–Liquid Flows. *AIChE J.* **2006**, *52*, 125–140. DOI:10.1002/aic.10611

[23] Xing, C.; Wang, T.; Wang, J. Experimental Study and Numerical Simulation with a Coupled CFD–PBM Model of the Effect of Liquid Viscosity in a Bubble Column. *Chem. Eng. Sci.* **2013**, *95*, 313–322. DOI:10.1016/j.ces.2013.03.022

[24] Sarhan, A.-R.; Naser, J.; Brooks, G. CFD Simulation on Influence of Suspended Solid Particles on Bubbles' Coalescence Rate in Flotation Cell. *Int. J. Miner. Process.* **2016**, *146*, 54–64. DOI:10.1016/j.minpro.2015.11.014

[25] Sarhan, A.-R.; Naser, J.; Brooks, G. CFD Analysis of Solid Particles Properties Effect in Three-Phase Flotation Column. *Sep. Purif. Technol.* **2017**, *185*, 1–9. DOI:10.1016/j.seppur.2017.04.042

[26] Sarhan, A.-R.; Naser, J.; Brooks, G. Effects of Particle Size and Concentration on Bubble Coalescence and Froth Formation in a Slurry Bubble Column. *Particuology* **2018**, *36*, 82–95. DOI:10.1016/j.partic.2017.04.011

[27] Sarhan, A.-R.; Naser, J.; Brooks, G. Bubbly Flow with Particle Attachment and Detachment – *A* Multi-Phase CFD Study. *Sep. Sci. Technol.* **2018**, *53*, 181–197. DOI:10.1080/01496395.2017.1375525

[28] Schiller, L.; Naumann, A. A Drag Coefficient Correlation. *Z. Ver. Dtsch. Ing.* **1935**, *77*, 318–320.

[29] Takamasa, T.; Tomiyama, A. Three-Dimensional Gas-Liquid Two-Phase Bubbly Flow in a C-Shaped Tube. Presented at the 9th International Topical Meeting on Nuclear Reactor Thermal Hydraulics, San Francisco, CA, Oct. 3, 1999.

[30] Tomiyama, A.; Shimada, N. A Numerical Method for Bubbly Flow Simulation Based on a Multi-Fluid Model. *J. Pressure Vessel Technol.* **2001**, *123*, 510–516. DOI:10.1115/1.1388010

[31] Tomiyama, A.; Tamai, H.; Zun, I.; Hosokawa, S. Transverse Migration of Single Bubbles in Simple Shear Flows. *Chem. Eng. Sci.* **2002**, *57*, 1849–1858. DOI:10.1016/S0009-2509(02)00085-4

[32] Frank, T.; Zwart, P.-J.; Krepper, E.; Prasser, H.-M.; Lucas, D. Validation of CFD Models for Mono- and Polydisperse Air–Water Two-Phase Flows in Pipes. *Nucl. Eng. Des.* **2008**, *238*, 647–659. DOI:10.1016/j.nucengdes.2007.02.056

[33] Laborde-Boutet, C.; Larachi, F.; Dromard, N.; Delsart, O.; Schweich, D. CFD Simulation of Bubble Column Flows: Investigations on Turbulence Models in RANS Approach. *Chem. Eng. Sci.* **2009**, *64*, 4399–4413. DOI:10.1016/j.ces.2009.07.009

[34] Yakhot, V.; Orszag, S.-A.; Thangam, S.; Gatski, T.-B.; Speziale, C.-G. Development of Turbulence Models for Shear Flows by a Double Expansion Technique. *Phys. Fluids. A* **1992**, *4*, 1510–1520. DOI:10.1063/1.858424

[35] Sato, Y.; Sekoguchi, K. Liquid Velocity Distribution in Two-Phase Bubble Flow. *Int. J. Multiphase Flow* **1975**, *2*, 79–95. DOI:10.1016/0301-9322(75)90030-0

[36] ANSYS. ANSYS Fluent 16.2 Documentation. ANSYS Inc., 2015.

[37] Luo, H.; Svendsen, H.-F. Theoretical Model for Drop and Bubble Breakup in Turbulent Dispersions. *AIChE J.* **1996**, *42*, 1225–1233. DOI:10.1002/aic.690420505

[38] Saffman, P.-G.; Turner, J.-S. On the Collision of Droplets in Turbulent Clouds. *J. Fluid Mech.* **1956**, *1*, 16–30. DOI:10.1017/S0022112056000020

[39] Abrahamson, J. Collision Rates of Small Particles in a Vigorously Turbulent Fluid. *Chem. Eng. Sci.* **1975**, *30*, 1371–1379. DOI:10.1016/0009-2509(75)85067-6

[40] Higashitani, K.; Yamauchi, K.; Matsuno, Y.; Hosokawa, G. Turbulent Coagulation of Particles Dispersed in a Viscous Fluid. *J. Chem. Eng. Japan.* **1983**, *16*, 299–304. DOI:10.1252/jcej.16.299

[41] Hagesaether, L.; Jakobsen, H.-A.; Svendsen, H.-F. A Model for Turbulent Binary Breakup of Dispersed Fluid Particles. *Chem. Eng. Sci.* **2002**, *57*, 3251–3267. DOI:10.1016/S0009-2509(02)00197-5

[42] Malloy, A.; Carr, B. Nanoparticle Tracking Analysis. *Part. Part. Syst. Charact.* **2006**, *23*, 197–204. DOI:10.1002/ppsc.200601031

[43] Filipe, V.; Hawe, A.; Jiskoot, W. Critical Evaluation of Nanoparticle Tracking Analysis (NTA) by NanoSight for the Measurement of Nanoparticles and Protein Aggregates. *Pharm. Res.* **2010**, *27*, 796–810. DOI:10.1007/s11095-010-0073-2

[44] Kolmogorov, A.-N. On the Breakage of Drops in a Turbulent Flow. *Dokl. Akad. Nauk. SSSR* **1949**, *66*, 825–828.

[45] Evans, G.-M.; Jameson, G.-J.; Atkinson, B.-W. Prediction of the Bubble Size Generated by a Plunging Liquid Jet Bubble Column. *Chem. Eng. Sci.* **1992**, *47*, 3265–3272. DOI:10.1016/0009-2509(92)85034-9

Nomenclature

α_q	volume fraction of the q^{th} phase;
ρ_q	density of the q^{th} phase, kg/m^3;
$\vec{u}_q$	velocity of the q^{th} phase, m/s;
p	pressure, Pa;
$\vec{g}$	gravity acceleration, m/s^2;
A_i	interfacial area, m^2;
C_D	drag coefficient;
Re_p	bubble Reynolds number;
σ	surface tension, N/m;

L	bubble diameter, m;
L_h	long axis of the deformable bubble, m;
C_l	lift force coefficient;
k	turbulent kinetic energy, m^2/s^2;
ε	turbulent dissipation rate, m^2/s^3;
σ_k	turbulent Prandtl numbers for k;
σ_ε	turbulent Prandtl numbers for ε;
μ_q	shear viscosity of phase q, Pa·s;
v_q	kinematic viscosity of phase q, m^2/s;
Ω_{ag}	aggregation kernel, m^3/s;
$\overline{u}_{ij}$	characteristic velocity of two colliding bubbles, m/s;
We	Weber number;
η	Kolmogorov microscale, m;
L_i	diameter of bubble i, m;
V_i	volume of bubble i, m^3;
n_i	number density of bubble i, $1/m^3$;
l	eddy size, m;
Ω_{br}	breakage kernel, $1/m^3/s$;
$N_{\text{pbm}}^{\text{outlet}}$	bubble number density at the outlet, 1/mL;
$N_{\text{pbm}}^{\text{tank}}$	bubble number density in the tank, 1/mL;
Q_{total}	flow rate, L/min;
$V_{\text{water}}^{\text{tank}}$	wate volume in the tank, L;
We_c	critical Weber number;
L_m	maximum stable bubble diameter, m;